

Programming tunable active dynamics in a self-propelled robot

Somnath Paramanick¹, Arnab Pal², Harsh Soni³, and Nitin Kumar^{1*}

¹*Department of Physics,
Indian Institute of Technology Bombay Powai,
Mumbai 400076, India*

²*The Institute of Mathematical Sciences,
CIT Campus, Taramani, Chennai 600113,
India & Homi Bhabha National Institute,
Training School Complex,
Anushakti Nagar, Mumbai 400094, India*

³*School of Physical Sciences,
Indian Institute of Technology Mandi, Mandi 175001, India*

(Dated: June 13, 2023)

We present a scheme for producing tunable active dynamics in a self-propelled robotic device. The robot moves using the differential drive mechanism where two wheels can vary their instantaneous velocities independently. This velocity data is first calculated by equating its equations of motion in two dimensions with well-established active particle models and later encoded into the robot's microcontroller. We demonstrate that the robot can depict active Brownian, run and tumble, and Brownian dynamics with a wide range of parameters. The resulting motion analyzed using particle tracking shows excellent agreement with the theoretically predicted trajectories. Moreover, as a function of external signals received through hardware components like light intensity and infrared sensors, the robot can modify its dynamics providing spatiotemporal control over its motion. We demonstrate our claims with an experiment where the robot searches for an object and brings it back to its origin point, reminiscent of foraging and homing behaviour observed in living organisms. This work opens an avenue for designing tunable active systems with the potential of revealing the physics of active matter and its application for bio- and nature-inspired robotics.

I. INTRODUCTION

Active matter refers to systems comprised of self-propelled particles that consume energy to perform mechanical work [1–4]. Such systems exhibit striking non-equilibrium phenomena such as collective dynamics, self-organization, and anomalous mechanical properties ubiquitous in the natural and biological world [5–17]. Over the past few decades, numerous analytical, numerical, and experimental studies have advanced our understanding of such systems. Yet we are just beginning to realize the potential of active matter in building smart, adaptable materials and autonomous devices [18–20]. Achieving this will require better control over individual particle dynamics and inter-particle interactions. Thus, many studies in recent years have reported concerted efforts to achieve programmable control on active matter spanning a broad range of length scales [21–32]. Here, we develop a novel active matter system consisting of a collection of smart programmable self-propelled robots capable of sensing their environment using onboard sensors. As a first step, in this paper, we present simple protocols for extracting tunable active dynamics in a single robot. We also demonstrate how our robot can execute the complex task of searching for an object and fetching it to a pre-determined location, reminiscent of the phenomenon of foraging and homing.

Previous studies have shown that emerging properties in active systems depend on the self-propulsion mechanism of individual agents, the strength of alignment interaction, and the nature of the surrounding medium [2]. Therefore, an artificial active material must incorporate all these features to replicate complex non-equilibrium properties displayed by active systems. Yet, broadly speaking, modeling individual constituent dynamics using simple theoretical frameworks of active Brownian particles (ABP) and run-and-tumble particles (RTP) has proven successful in replicating emerging phenomena with great success [3]. Thus, a robotic device, due to its programmability becomes a natural choice to mimic controlled active particle dynamics. While there are many examples in the literature where robots perform programmable complex self-assembly [33] as well as spontaneous collective behavior [34–37] they rely on vibration motors for locomotion [33–35]. More recently, differential drive robots have also been reported which show much better control of individual dynamics [26, 38–40]. Yet, a detailed protocol to program them with well-established theoretical models of ABP, RTP, and Brownian particle (BP) is missing.

In this work, we present a robotic system that displays a variety of active dynamics with many controllable parameters. Our robot is circularly shaped and propels itself using the differential drive mechanism. In addition, the robot also houses hardware components like multiple infrared (IR) and light intensity (LI) sensors which help it detect environmental factors like obstacles and ambi-

* nkumar@iitb.ac.in

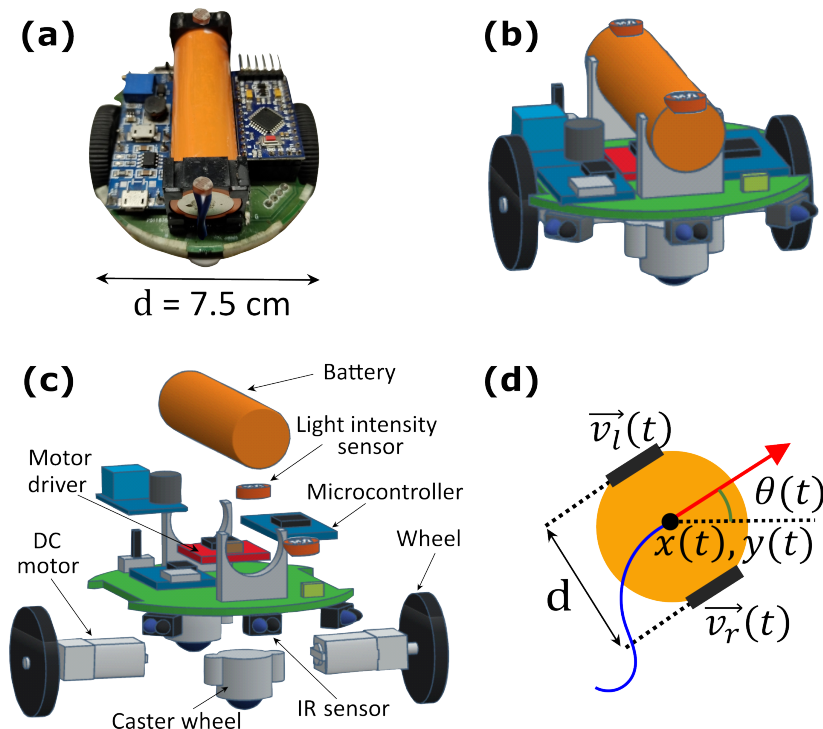


FIG. 1. **Robot model:** (a) The robot used in the experiment with its diameter indicated. (b) A schematic representation of the same robot. (c) An expanded view highlighting its important hardware components. (d) Robot's position $(x(t), y(t))$ and orientation $\theta(t)$ vary as a function of the instantaneous left and right wheel's velocities $(v_l(t)$ and $v_r(t)$, respectively), resulting in the centre of mass tracing out a trajectory indicated by the blue solid line.

ent light. We show that with its two wheels oppositely placed at a diameter distance away, its center of mass can display a variety of motions depending entirely on the instantaneous wheel velocities. Firstly, we show our results on the following three models: (i) Active Brownian particle (ABP) with and without translational noise, (ii) Run and Tumble particle (RTP), and (iii) Brownian particle (BP) dynamics. These results are found to be in excellent agreement with our theoretical modeling. We also show that the robot can be appropriately programmed to react to environmental factors like ambient light intensity gradients. This key feature is showcased by letting the robot demonstrate a complex task that resembles an active foraging and homing behavior. Here, a robot searches, captures, and fetches back a payload to a predetermined location marked by the highest intensity region by following an external light-intensity gradient field. Taken together, our results propose a novel experimental system based on smart programmable robots that provide an ideal platform for exploring problems related to active and living systems with potential in future material design.

II. ROBOT MODEL

Our robot is a circularly shaped electronic gadget with a diameter of 7.5 cm and a height of 5 cm (See Fig. 1(a-

c)). It is assembled using various hardware components as indicated in Fig. 1(c). It has two rubber wheels of diameter 3.3 cm placed at the two ends of its diameter. Two caster wheels are placed in the perpendicular direction for support. It also carries six IR sensors symmetrically placed along the circumference to detect obstacles. Two light intensity (LI) sensors, each placed at the front and back, enable the robot to detect light intensity gradients along an axis parallel to its wheels. We use the differential drive technique for the robot's movement on a 2D plane surface by controlling the velocity of the wheels independently [41]. The programs, written using Arduino IDE software, are loaded onto an Arduino pro mini microcontroller board (3.3 V, 8 MHz version), and the output signal is fed to the motor driver (Dual TB6612FNG by SparkFun), that rotates the wheels using two separate DC motors. The signal from the microcontroller provides 256 different analog voltage levels from zero to maximum voltage (5V) to the motors. This gives each wheel a range of velocities maximum of up to 27 cm/sec. All these components are powered using a Li-ion battery. A brief summary of robot functioning is presented in SI Fig.1. The robot performs its dynamics on a flat surface of dimensions 90 cm \times 120 cm with a white background. We use an overhead projector connected to a computer to illuminate the surface with desired intensity profile. We capture the dynamics of the robot using a high-speed camera from the top and

perform image analysis to extract instantaneous position and orientation. (See Appendix A).

We begin by writing the equations of motion of the robot in two dimensions. Let $v_l(t)$ and $v_r(t)$ be the velocities of the left and right wheels of the robot along its orientation at time t (See Fig. 1(d)). Then the equations of motion for the position $(x(t), y(t))$ and the orientation angle $\theta(t)$ of the robot read

$$\begin{aligned}\dot{x}(t) &= \frac{v_l(t) + v_r(t)}{2} \cos \theta(t), \\ \dot{y}(t) &= \frac{v_l(t) + v_r(t)}{2} \sin \theta(t), \\ \dot{\theta}(t) &= \frac{v_r(t) - v_l(t)}{d},\end{aligned}\quad (1)$$

where d is the diameter of the robot, and the dot stands for the time derivative. We next show that purely based on the instantaneous values of v_l and v_r , we can program the robot to perform desired stochastic dynamics.

III. RESULTS AND DISCUSSION

A. ABP model without translational noise

A distinctive feature of a polar active particle is its finite self-propulsion speed. In general, it can have rotational as well as translational noise. We first study the case without an explicit source of translational noise. In that case, it is often modeled as an ABP, which is equivalent to a biased random walk in two dimensions where the particle always moves in the direction of its instantaneous orientation. Consequently, the ABP moves with a constant speed but its direction changes randomly in the plane. The dynamics of an ABP of speed v is governed by the following equations of motion:

$$\begin{aligned}\dot{x}(t) &= v \cos \theta(t), \\ \dot{y}(t) &= v \sin \theta(t), \\ \dot{\theta}(t) &= \zeta(t),\end{aligned}\quad (2)$$

where ζ is the instantaneous rotational speed of the ABP; it is a white noise with a zero mean and is often modeled as white Gaussian noise. Here we construct an active Brownian robot with ζ having a uniform distribution between $[-\eta, \eta]$. In order to produce an ABP motion of given η and v in our robot, we compare (2) and (1) to obtain the expressions of v_l and v_r , which yields

$$\begin{aligned}v_l(t) &= \frac{2v + \zeta(t)d}{2}, \\ v_r(t) &= \frac{2v - \zeta(t)d}{2}.\end{aligned}\quad (3)$$

The values of v_l and v_r are updated in the robot after every ϵ seconds, termed as delay time. In experiments, the accessible values of parameters η and ϵ lie between 1 - 6 rad/s and 0.1 - 0.9 s, respectively.

When implemented in the robot, it mimics the ABP motion quite well. A typical trajectory of the robot is shown in Fig. 2(a) and SI movie S1. To get this unbounded free particle trajectory, we use boundary wall detection using IR sensors to remove the confinement effects (See Appendix B). The zoomed-in part of the trajectory ascertains the absence of translational noise at short time scales. The mean squared displacement (MSD) shows a transition from ballistic to diffusive behavior, a hallmark feature of the ABP dynamics (see Fig. 2(b)). Using a simple theoretical calculation, we obtain the following expression for the MSD [42, 43]

$$\langle \Delta r^2(\tau) \rangle = \frac{2v^2}{D_r} \left[\tau + \frac{1}{D_r} (e^{-D_r \tau} - 1) \right], \quad (4)$$

where $D_r = \epsilon \langle \zeta^2 \rangle / 2 = \epsilon \eta^2 / 6$ (see Appendix C). The solid red line in Fig. 2(b) represents analytically obtained MSD, which shows an excellent agreement with our experimental data. We further plot angular MSD defined as $\langle \Delta \theta^2(\tau) \rangle$ for varying ϵ and η independently (See Figs. 2(c) and 2(d)). Interestingly, we find that it scales linearly with τ only for $\tau > \epsilon$ whereas for $\tau < \epsilon$, the plot is ballistic with τ^2 scaling. This happens because during the time duration ϵ , the robot always rotates with a constant angular velocity of magnitude $|(v_l - v_r)/d|$ resulting in $\Delta \theta$ scaling linearly with τ . For given ϵ and η , the experimental value of D_r is measured by line-fitting $\langle \Delta \theta^2(\tau) \rangle$, using the formula $\langle \Delta \theta^2(\tau) \rangle = 2D_r \tau$. We then plot D_r as a function of ϵ and η in the insets of Figs. 2(c) and 2(d), respectively, showing D_r indeed scaling according to the expression $D_r = \epsilon \eta^2 / 6$, as predicted by the theory.

We also measure spatial velocity autocorrelation function, $C(l) = \langle \mathbf{v}(r) \cdot \mathbf{v}(r+l) \rangle_r / v^2$, where r is the distance traveled by the robot, with respect to l for different values of η keeping ϵ constant at 0.25 s as shown in Fig. 2(e) inset. We find that $C(l) \propto e^{-l/L_s}$, where L_s is the persistence length. Using the above relation, we extracted L_s for different η . We find that L_s decreases algebraically with η with an exponent of “-2”. This also agrees with the theory since $L_s = v/D_r \propto \eta^{-2}$.

B. ABP model with translational noise

In general, at small time scales, a polar particle may have translational noise along as well as normal to its orientation. In this case, therefore, v in (2) is not a constant and rather fluctuates around its mean value. We achieve this by generating $v_l(t)$ and $v_r(t)$ from two statistically independent random uniform distributions in a range of $2V$ with a finite mean v_a , i.e., in the interval $[v_a - V, v_a + V]$. Here V quantifies the strength of the translational noise. Interestingly, since our robot, at any instance, can only move along the direction of its wheels, this noise features only in the velocity component, which is parallel to its orientation, while noise normal to its orientation is forbidden. As a result, both $\dot{\theta}(t)$ and $v(t)$

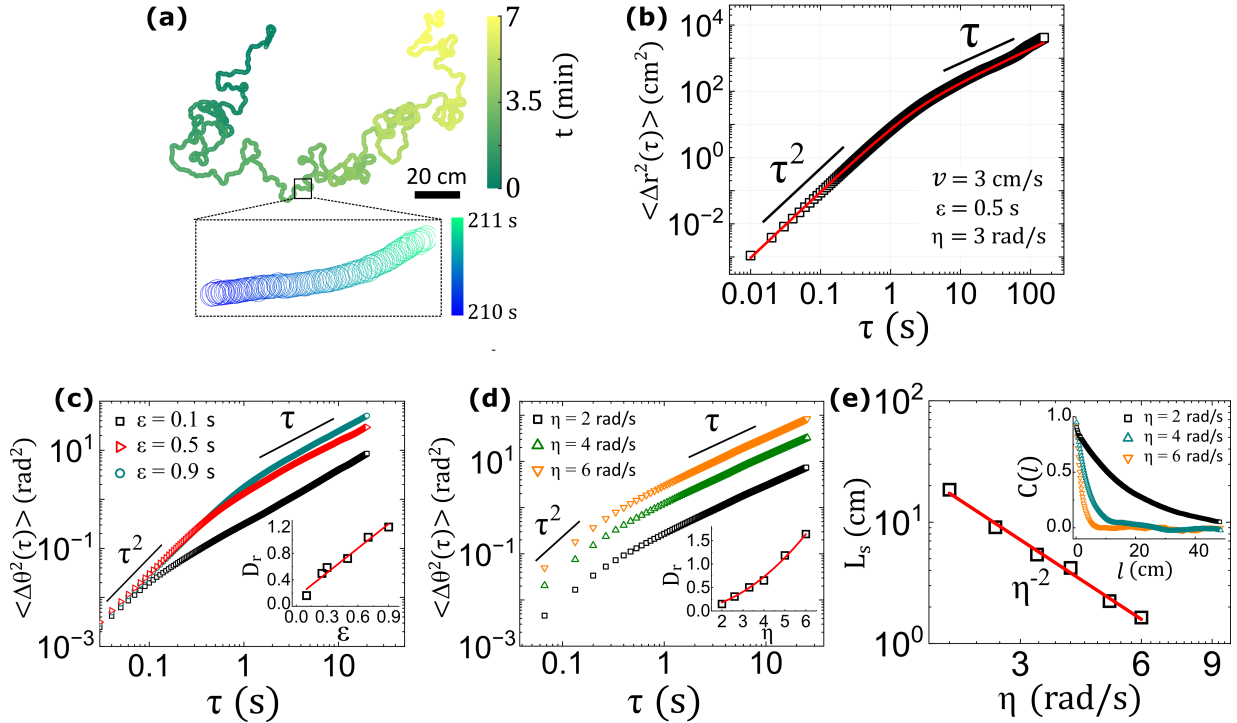


FIG. 2. **ABP model without translational noise:** (a) A typical trajectory of the robot following ABP dynamics with velocity $v = 3$ cm/s, delay time $\epsilon = 0.5$ s, and rotational noise $\eta = 3$ rad/s. The color bar represents the time. The zoomed-in portion of the trajectory shows the robot moving with a constant velocity at all time steps, indicative of the absence of translational noise at short time scales. (b) Translational mean-square displacement (MSD) of the trajectory plotted as a function of time τ showing a ballistic ($\sim \tau^2$) to diffusive ($\sim \tau$) transition. The solid line shows the fit with the analytical expression given by (4). (c) Angular MSD, $\langle \Delta \theta^2(\tau) \rangle$, plotted for three values of ϵ keeping $\eta = 3$ rad/s. $\langle \Delta \theta^2(\tau) \rangle$ also undergoes a ballistic to diffusive transition at time ϵ . (Inset) The experimental values of D_r , measured by line fitting the linear part of the MSD, show linear scaling with ϵ . (d) Angular MSD as a function of τ for different values of η keeping ϵ fixed at 0.25 s. (Inset) D_r extracted from the plots increases quadratically with η . (e) Persistence length L_s shows an algebraic decay with η with an exponent consistent with theory. L_s is extracted by fitting an exponential function to the spatial velocity autocorrelation function, $C(l) = \langle \mathbf{v}(r) \cdot \mathbf{v}(r+l) \rangle_r / v^2$ shown in the inset.

become random variables with zero and a non-zero mean ($= v_a$), respectively.

Fig. 3(a) and SI movie S2 show a typical trajectory of the robot following noisy ABP dynamics. At long time scales, the trajectory qualitatively looks similar to the ABP without translational noise (Fig. 2(b)) but differs significantly at short time scales as depicted by frequent back-and-forth events in the zoomed-in trajectory. We plot experimentally measured MSD in Fig. 3(b), which shows scaling with τ at both short and very long time scales as reported in past studies [43]. We solve the Langevin equation for this case and obtain the following expression of the MSD

$$\langle \Delta r^2(\tau) \rangle = 2D_t\tau + \frac{2v_a^2}{D_r^2} [D_r\tau + (e^{-D_r\tau} - 1)], \quad (5)$$

where $D_t = \epsilon V^2/12$ and $D_r = \epsilon V^2/3d^2$ are the translational and the rotational diffusion constants, respectively (see Appendix C). Again the experimental data agree well with the analytical MSD expression (solid red line) over the entire range of time scales (Fig. 3(b)).

Clearly, in the limits $\tau \rightarrow 0$ and $\tau \rightarrow \infty$, (5) reduces to $\langle \Delta r^2(\tau) \rangle_{\tau \rightarrow 0} = 2D_t\tau$ and $\langle \Delta r^2(\tau) \rangle_{\tau \rightarrow \infty} = 2(D_t + v_a^2/D_r)\tau$, respectively, showing an agreement with our experimental results.

C. Brownian particle model

A Brownian particle (BP) in two dimensions can move in any direction with an equal probability. However, quite obviously, the wheels of our robot can move only along its direction of orientation, not normal to it. Here we show that it is possible for our robot to perform BP dynamics with limited movement of its wheels. Notably, the ABP motion with noise described in the previous section reduces to the BP dynamics when $v_a = 0$. As a result, both $v(t)$ and $\dot{\theta}$ become random variables with zero mean. Fig. 3(c) and SI movie S3 show the trajectory of the robot following the BP model with $V = 7$ cm/s and $\epsilon = 0.2$ s. The resulting MSD shows that at short times ($< \epsilon$) the motion is ballistic, and at longer times it

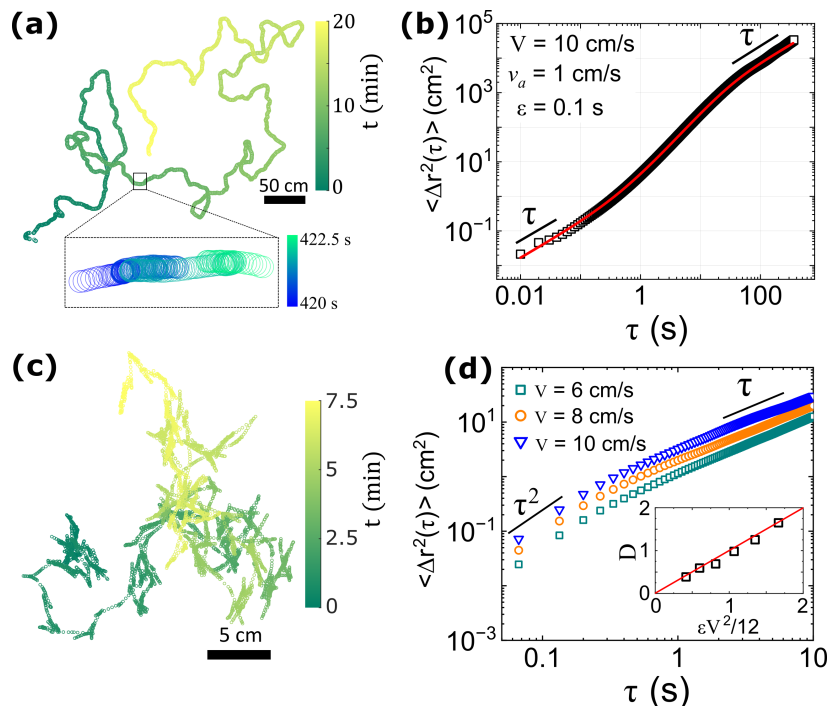


FIG. 3. **ABP model with translational noise and BP model:** (a) Typical trajectory of the robot programmed to follow ABP model with translational noise having $V = 10$ cm/s, $\epsilon = 0.1$ s, and $v_a = 1$ cm/s. The color bar represents the time. The zoomed-in trajectory shows the presence of translational noise in the form of significant back-and-forth events along the robot's orientation. (b) The translational MSD shows a diffusive to super-diffusive to diffusive transition as a function of time. The solid line is fit with the analytical expression given by (5). (c) A typical trajectory of the robot following a BP motion with $V = 7$ cm/s, $\epsilon = 0.2$ s, and $v_a = 0$ cm/s. The color bar represents the time of motion. (d) The translational MSD of the BP motion plotted for three values of V keeping ϵ fixed at 0.2 s shows a ballistic to diffusive transition. The ballistic motion is a consequence of the finite delay time ϵ which also sets the crossover time for all the curves. The inset shows the diffusion constant D measured from the MSD curves matches with $\epsilon V^2/12$ as predicted by the theory.

is diffusive (see Fig. 3(d)), similar to $\langle \Delta \theta^2(\tau) \rangle$ observed in Figs. 2(c) and 2(d). Again, the ballistic regime is a consequence of finite velocity events experienced by both left and right wheels over a time interval of ϵ . This is further verified by the fact that the crossover from ballistic to diffusive regime happens exactly after ϵ .

Moreover, since $\langle \Delta r^2(\tau) \rangle = 2D\tau$, we extract the diffusion constants D from the MSD plots for various values of V and ϵ . We plot this value with the analytical result, which predicts $D = \epsilon \langle v^2 \rangle / 2 = \epsilon V^2 / 12$ in Fig. 3(d). Clearly, we find an excellent agreement with the theory (solid line indicating the equality).

D. Run and tumble particle model

We now turn our attention to the RTP models, where an individual particle moves in a straight line interrupted by frequent tumble events that randomize its run direction (Fig. 4(a)) [44, 45]. Such motion is widely observed in micro-organisms like bacteria [46] and even in active granular particles [47]. In the case of our robot, it runs when the left and right wheels have the same velocities, i.e., $v_l = v_r = v_{\text{run}}$, and it tumbles to a new direction

when $v_l = -v_r$. A typical trajectory of the robot performing RTP motion is shown in Fig. 4(b) and SI movie S4 with its instantaneous speed plotted in Fig. 4(c). Here, the robot runs with a constant speed v_{run} for a duration τ_r (run time), after which it tumbles over a time τ_t (tumble duration). It is important to highlight that τ_t can never be zero in our experiments since the robot can never tumble instantaneously. Inspired by the experimental observations in bacteria [46], we choose τ_r from an exponential distribution $P(\tau_r) = \gamma e^{-\gamma \tau_r}$, whereas τ_t is kept constant for all tumble events. This is achieved by scaling the tumble speed with the tumble angle, which is chosen randomly between 0 to 360 degrees. The RTP trajectory shown in Fig. 4(b) has $v_{\text{run}} = 5$ cm/s, $\gamma = 3$, and $\tau_t = 0.5$ s. Later we perform experiments for various τ_r distributions characterized by γ at fixed $\tau_t = 0.5$ s. The resulting MSD is shown in Fig. 4(d), showing a ballistic ($\sim \tau^2$) to diffusive ($\sim \tau$) transition with transition time decreasing as we increase γ . However, when we vary τ_t while keeping γ constant (Fig. 4(e) for $\gamma = 1$ s⁻¹), the transition time remains independent of τ_t . Regardless, the MSD measured experimentally shows an excellent agreement with the theoretical expression given

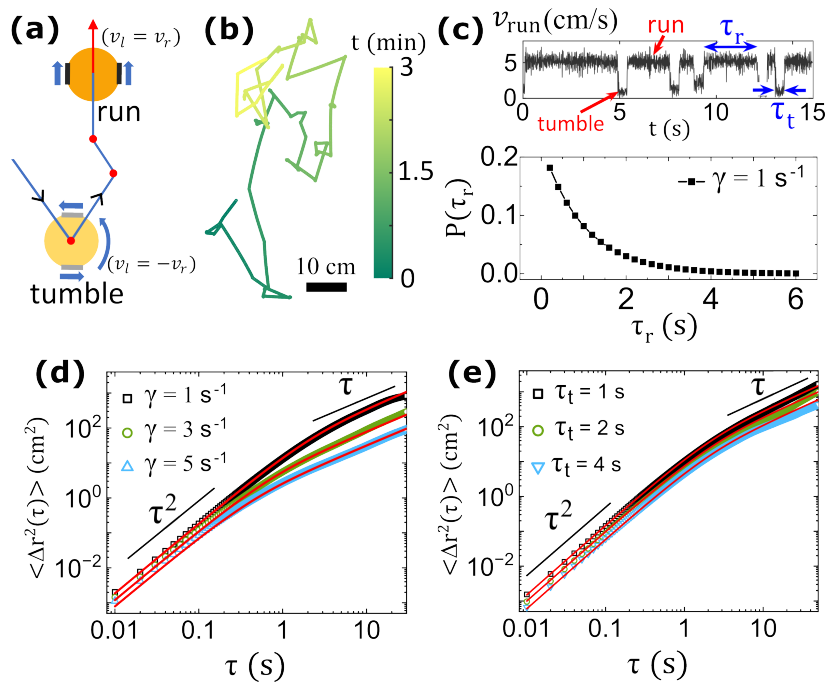


FIG. 4. **RTP model:** (a) A typical schematic of the robot mimicking RTP model. A run event is characterized by a straight trajectory when $v_l = v_r$. The robot tumbles while $v_l = -v_r$ and finds a new run direction randomly. (b) The trajectory of the robot for a duration of 3 minutes, programmed to follow RTP model. The color bar shows the time. (c) The top plot shows the instantaneous speed of the robot, which switches between $v_{\text{run}} = 5$ cm/s and $v_{\text{run}} = 0$, representing run and tumble, respectively. τ_r and τ_t represent run and tumble duration, respectively. τ_t is constant during the motion, whereas τ_r is extracted from an exponential distribution $P(\tau_r) = \gamma e^{-\gamma \tau_r}$ as shown in the bottom plot. Parameter values for the trajectory shown in (b) are $v_{\text{run}} = 5$ cm/s, $\gamma = 3$, and $\tau_t = 0.5$ s. (d) Translational MSD as a function of time for three different γ values keeping $\tau_t = 0.5$ s. Solid pink lines are the fit with the theoretical expression given by (6). (e) Translational MSD for three different τ_t values keeping the τ_r distribution fixed with $\gamma = 1$. Again, solid lines represent the fit with the same theoretical expression.

by [48]

$$\langle \Delta r^2(\tau) \rangle = \frac{1}{1 + \gamma \tau_t} \frac{2v_{\text{run}}^2}{\gamma^2} (\gamma \tau - 1 + e^{-\gamma \tau}). \quad (6)$$

The solid red lines in Fig. 4(d) and (e) show the fit, which is in excellent agreement with the experimental results.

We further emphasize that we can also program our robot to become light-responsive and modify its dynamics as a function of the intensity of light falling on its LI sensors. We summarize this result in SI movie S5 where a robot is programmed to display BP, ABP, and RTP motion as a function of increasing light intensity.

E. Active foraging and homing

Finally, we apply the ideas developed so far to mimic a complex behavior of foraging and homing observed in living organisms [49–51]. Simply put, we intend the robot to autonomously search and capture a payload, which we term foraging, and retrieve it to its starting point, which we call homing [52]. The robot is confined inside an illuminated region which is a circle of diameter 1 m

(Fig. 5(a), SI movie S6). The intensity of light (measured in lux) decreases radially at a rate ∇I (inset plot). Point H, which we refer to as home, lies at the centre of the circle, which is also the brightest point in the plane. During the search phase, the robot starts from point H and performs an ABP motion without translational noise with $v = 10$ cm/s and $D_r = 0.15$ rad²/s as shown in Fig. 5(b). To avoid the robot's escape, we program it to reflect from the boundary wall, indicated with a red dashed line, beyond which there is a sharp fall in the light intensity. Such reflection events can be seen in the particle trajectory in Fig. 5(b) and (c). During the search phase, the robot's IR sensors continuously emit IR radiation. The payload is deemed searched when the robot is close enough to detect the reflected IR signal with the robot now pushing onto the payload due to its persistent ABP motion. Additionally, the concavity of its surface makes sure that the robot remains locked to it, a phenomenon that is equivalent to the funnel trapping of active particles reported in the past [47, 53, 54]. At the same moment, the robot also activates its front and back LI sensors, indicated by orange dots. The robot is now set to perform the homing motion shown by the blue trajectory in Fig. 5(d). While homing, the robot uses its LI

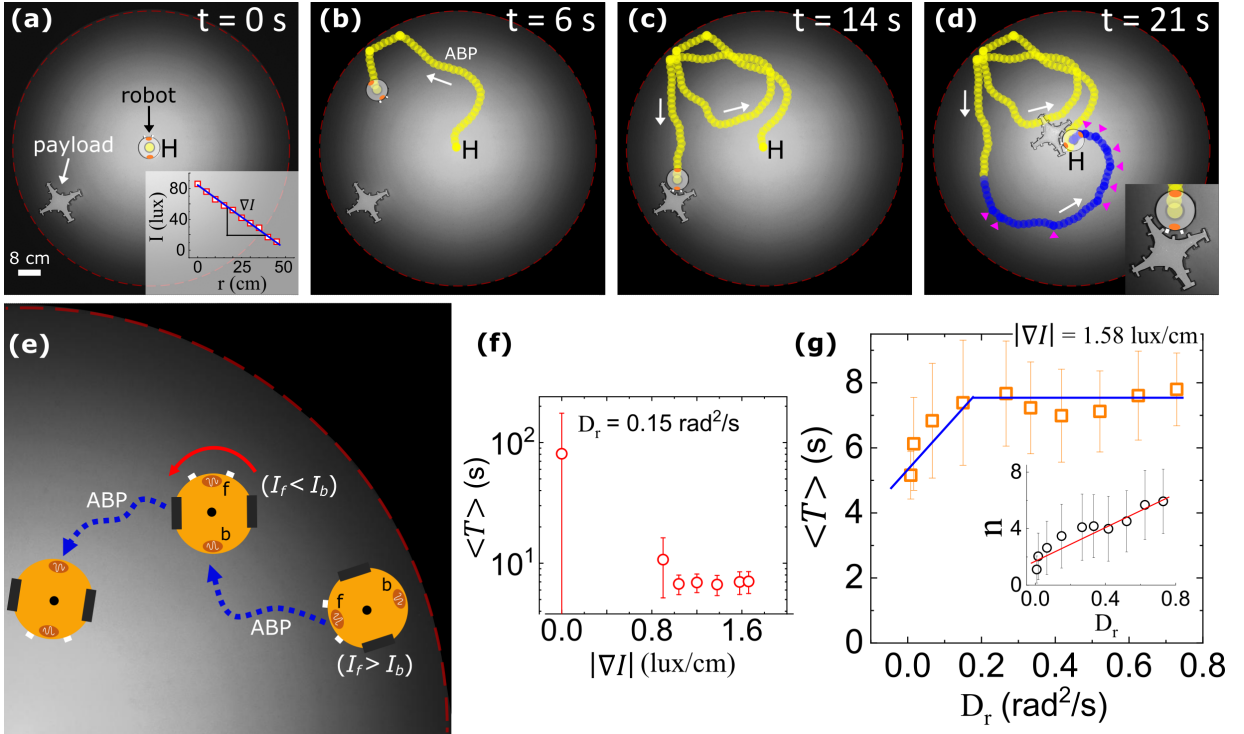


FIG. 5. Active Foraging and Homing: (a) A robot is placed at the centre (point H) of a circle of radius 50 cm. Orange dots on the robot represent LI sensors, and white dots in front of the robot are fangs that serve the purpose of capturing the payload. The region is lit by a radially symmetric light-intensity gradient field of magnitude ∇I (inset) with the maximum intensity at point H. The red dashed line at the circumference defines the boundary, which is characterized by a sudden fall in intensity. The payload is randomly placed at the boundary. The payload surface has multiple cogs, which are tooth-like structures, as shown. (b) The robot performs an ABP motion without translational noise (yellow trajectory, $v = 10$ cm/s and $D_r = 0.15$ rad²/s) and searches for the obstacle randomly. To avoid the robot escaping the region, we program it to reflect from the boundary with two typical reflection events indicated in the trajectory. (c) After a certain time and multiple reflections from the boundary, the robot detects the payload through its front IR sensors. This also activates the robot's LI sensors to detect the gradient field. (d) The return trajectory (blue line) is the same as the search ABP motion except for the condition that every time the robot points in the direction of decreasing intensity, it undergoes reorientation until it again points towards increasing intensity. Magenta arrowheads along the blue trajectory represent such events. Throughout the return phase, the robot's fangs remain interlocked to the payload's cogs, as shown in the inset. (e) A detailed schematic of a typical reorientation event. f and b indicate the front and the back LI sensors with intensity readings of I_f and I_b , respectively. If during the journey $I_f < I_b$, the robot undergoes a reorientation represented with a red arrow until $I_f > I_b$ again. (f) The mean return time $\langle T \rangle$ averaged over 100 experiments is fundamentally similar to the search time when $\nabla I = 0$ but decreases drastically once $|\nabla I| \neq 0$, during which $\langle T \rangle$ remains statistically independent of $|\nabla I|$. Error bars are equal to the standard deviation (SD). (g) $\langle T \rangle$, averaged over 100 experiments with error bars equal to the SD, increases linearly with D_r up to a certain value beyond which it becomes statistically constant. The solid lines represent guidelines. Inset shows the plot of the number of reorientation events, n , described in (e), which shows a linear increase with D_r . This indicates that beyond certain D_r , the return path is dominated by the light gradient-induced reorientation events rather than the fluctuations D_r of the motion.

sensors to detect the local light intensity at its front and back sensors, I_f and I_b , respectively. (Fig.5(e)). While $I_f > I_b$, the robot continues to perform the ABP motion. However, when $I_f < I_b$, the robot reorients itself (red arrow in Fig. 5(e)) until $I_f > I_b$ again and resumes its ABP motion (see SI movies S6 and S7). Such a behaviour is prevalent in cellular organisms like E. Coli and is known as klinokinesis [55]. While reorientation, the two fangs on the robot get interlocked to the cogs on the payload surface and ensure that it always remains attached to the robot (inset of Fig. 5(d)). The process continues until the robot reaches point H, with a blue line indicating

the complete return trajectory. The magenta arrowheads indicate reorientation events (Fig. 5(d)).

We believe that the intensity gradient acts as an equivalent of *cognitive memory* in the robot which it uses to return home efficiently. This is evidenced by the fact that whereas average return time $\langle T \rangle$ is significantly higher without the light gradient, it decreases sharply when $|\nabla I| \neq 0$ as shown in Fig. 5(f). We also find that $\langle T \rangle$ for $|\nabla I| = 0$ is similar to the search time as expected. However, quite remarkably, we find that $\langle T \rangle$, measured over 100 experiments with payload always kept at the boundary, increases linearly with D_r initially but saturates to a

fixed value of ≈ 8 s beyond critical $D_r \approx 0.2$ rad²/s (see Fig. 5(g)). To elucidate this intriguing behavior, we plot the average number of tumble events n during the return phase for various D_r values in the inset of Fig. 5(g). We find that n increases linearly with D_r , indicating that a less persistent motion of the robot is compensated by an increased number of reorienting events. This results in an almost persistent and near-deterministic motion toward home which might explain the saturation of $\langle T \rangle$ observed in our experiments. In other words, the memory of the robot, via intermittent reorientations toward the gradient intensity, optimizes the return time and becomes independent of its inherent stochastic noise D_r . This is also evocative of the resetting phenomenon in the context of search strategies [52, 56–59]. Detailed exploration is required to uncover the possible similarities between these phenomena, which we leave for future work.

IV. CONCLUSION

Here, we introduced a novel experimental system consisting of self-propelled robots. These robots are essentially smart computing devices capable of executing a preloaded program and simulating it to in-plane dynamics with excellent control. Using hardware components like IR and LI sensors, they can also detect obstacles and ambient light intensity and modify their motion as required. The robots are driven by two wheels placed diametrically opposite to each other and move independently with velocities v_l and v_r , respectively. We first show that instantaneous values of v_l and v_r calculated from scalar active particle models like Active Brownian, Run and Tumble, and Brownian motion reproduce desired stochastic dynamics in the centre of mass of the robots quite accurately. The experimental parameter space over which this motion can be tuned is quite exhaustive and highly tunable. We also demonstrated the control over robot motion using ambient light as an external control parameter. Finally, we applied a combination of robot programmability and sensitivity to its surroundings to replicate a complex task of searching, capturing, and fetching a payload to a predetermined location, a phenomenon that resembles active foraging and homing ubiquitous in the animal world. We used a light-gradient pattern to aid the robot’s return phase, which we argue is a measure of the robot’s cognitive memory. Interestingly, we observe that the environmental memory can expedite the successful homing of a payload or a target utilizing the inherent noise of the robot.

Overall, the experimental system presented in this paper holds great potential in unraveling laws governing the non-equilibrium physics of active and living systems with applications to smart and adaptive material design. The next step is to use a collection of such robots, which offer a significant advantage over already existing experimental systems due to our ability to control individual dynamics with great control. Moreover, we can also engen-

der complex inter-robot interaction using IR and LI sensors which can test not only existing theories in the field but also can generate novel dynamical phases hitherto unknown. Furthermore, a collection of such robots also offer possible applications for bio-inspired and nature-inspired robotics.

ACKNOWLEDGEMENTS

NK acknowledges financial support from DST-SERB for CRG grant number CRG/2020/002925 and IITB for the seed grant. NK also thanks Sriram Ramaswamy and Sanjib Shabhapanidit for productive discussions. AP acknowledges research support from the DST-SERB Start-up Research Grant Number SRG/2022/000080 and the Department of Atomic Energy. HS acknowledges SERB for the SRG (grant no. SRG/2022/000061-G). SP thanks CSIR India for research fellowship.

APPENDIX A: Image-analysis technique

In experiments on modeling the robot dynamics, we attach two filled black circles, one bigger than the other, on top of the robot along the robot orientation. We then use MATLAB’s blob analysis to extract their position coordinates. The vector connecting them provides the instantaneous orientation of the robot, and the midpoint of the line connecting them provides the center-of-mass coordinate. The frame rate at which movies are captured varies between 10-100 depending on the robot’s speed. The movies are captured for a duration of 1 hour for each model. For foraging and homing experiments, we only use one circle to detect the robot’s instantaneous position.

APPENDIX B: Removing confinement effect

Theoretical models of ABP, RTP, and BP dynamics consider an unbounded motion of the particle. In our experiments, we use the following protocol to remove confinement effects caused by boundary walls. Once the robot detects the boundary through its IR sensors, it moves 40 cm in the reverse direction while maintaining its orientation. Later, we remove these straight trajectories from the experiments and stitch all the stochastic tracks together by shifting the coordinates appropriately (See Fig.2 in SI). This creates a continuous free particle motion that is effectively unconfined.

APPENDIX C: Theoretical calculation

1. ABP model without translational noise

In general, the equations of motion for the robot are given by

$$\dot{x}(t) = v(t) \cos \theta(t), \quad (7a)$$

$$\dot{y}(t) = v(t) \sin \theta(t), \quad (7b)$$

$$\dot{\theta}(t) = \zeta(t), \quad (7c)$$

where $v(t)$ is the component of the instantaneous robot velocity along its orientation $\mathbf{n} = (\cos \theta(t), \sin \theta(t))$. The values of v and ζ are varied discretely with the step size of ϵ second. For mimicking the ABP model, v is kept constant and $\zeta(t)$ is chosen to be a random number with a uniform distribution between $[-\eta, \eta]$. For the time scales much larger than ϵ ,

$$\langle \zeta(t) \zeta(t') \rangle = 2D_r \delta(t - t'), \quad (8)$$

where D_r is the rotational diffusion constant. It is straightforward to show that [60]

$$\langle [\theta(\tau) - \theta(0)]^2 \rangle = 2D_r \tau. \quad (9)$$

Here the angular bracket represents the ensemble average. Whereas, from the discrete form of (7c),

$$\theta(\tau) = \theta(0) + \epsilon \sum_{i=1}^{N_\tau} \zeta_i, \quad (10)$$

where $\zeta_i \equiv \zeta(i\epsilon)$ and $N_\tau = \tau/\epsilon$. As the random number ζ_i has the uniform probability distribution between $[-\eta, \eta]$,

$$\langle \zeta_i \zeta_j \rangle = \delta_{ij} \frac{\eta^2}{3}. \quad (11)$$

Then, from (10),

$$\begin{aligned} \langle [\theta(\tau) - \theta(0)]^2 \rangle &= \epsilon^2 \sum_{i=1}^{N_\tau} \sum_{j=1}^{N_\tau} \langle \zeta_i \zeta_j \rangle \\ &= \epsilon^2 \sum_{i=1}^{N_\tau} \langle \zeta_i^2 \rangle \\ &= \epsilon^2 N_\tau \frac{\eta^2}{3} \\ &= \epsilon \tau \frac{\eta^2}{3} \end{aligned} \quad (12)$$

Comparing the above equation with (9), we obtain

$$D_r = \epsilon \frac{\eta^2}{6}. \quad (13)$$

2. ABP with translational noise

In this case, $v(t)$ in (7) is not constant, it rather fluctuates around its mean value. The values of $v(t)$ and $\zeta(t)$ in terms of the velocities of the left and right wheels of the robot, v_l and v_r , are given by

$$v(t) = \frac{v_r(t) + v_l(t)}{2}, \quad (14a)$$

$$\zeta(t) = \frac{v_r(t) - v_l(t)}{d}, \quad (14b)$$

where d is the diameter of the robot. Here v_l and v_r are statistically independent random numbers with a uniform probability distribution in the range $[v_a - V, v_a + V]$. Then, one can readily show that

$$\langle v_r(i\epsilon) v_r(j\epsilon) \rangle = \delta_{ij} \frac{V^2}{3} + v_a^2, \quad (15)$$

$$\langle v_l(i\epsilon) v_l(j\epsilon) \rangle = \delta_{ij} \frac{V^2}{3} + v_a^2, \quad (16)$$

$$\langle v_r(i\epsilon) v_l(j\epsilon) \rangle = 0. \quad (17)$$

Then the relations (14) give

$$\langle v(i\epsilon) v(j\epsilon) \rangle = \delta_{ij} \frac{V^2}{6} + v_a^2, \quad (18)$$

$$\langle \zeta(i\epsilon) \zeta(j\epsilon) \rangle = \delta_{ij} \frac{2V^2}{3d^2}, \quad (19)$$

$$\langle v(i\epsilon) \zeta(j\epsilon) \rangle = 0. \quad (20)$$

For the time scales much larger than ϵ , it is obvious from (18) that

$$\langle v(t) v(t') \rangle = 2D_t \delta(t - t') + v_a^2, \quad (21)$$

and ζ follows the correlation relation given by (8). Following the similar steps as done in Sec IV 1, one can show that

$$D_r = \frac{\epsilon V^2}{3d^2}, \quad (22)$$

$$D_t = \frac{\epsilon V^2}{12}. \quad (23)$$

The mean square displacement can then be calculated as follows

$$\begin{aligned} \Delta r^2(\tau) &= \langle [\mathbf{r}(\tau) - \mathbf{r}(0)] \cdot [\mathbf{r}(\tau) - \mathbf{r}(0)] \rangle \\ &= \left\langle \int_0^\tau dt \int_0^\tau dt' v(t) v(t') \cos [\theta(t) - \theta(t')] \right\rangle \\ &= \int_0^\tau dt \int_0^\tau dt' \langle v(t) v(t') \cos [\theta(t) - \theta(t')] \rangle \end{aligned} \quad (24)$$

As v and ζ are statistically independent of each other [from (20)], we have

$$\Delta r^2(\tau) = \int_0^\tau dt \int_0^\tau dt' \langle v(t) v(t') \rangle \langle \cos [\theta(t) - \theta(t')] \rangle.$$

Using (21) and the following relation [42, 61–63]

$$\langle \cos [\theta(t) - \theta(t')] \rangle = \exp(-D_r |t - t'|), \quad (25)$$

we arrive at

$$\begin{aligned} \Delta r^2(\tau) &= \int_0^\tau dt \int_0^\tau dt' \left\{ [2D_t \delta(t - t') + v_a^2] \right. \\ &\quad \left. \times \exp(-D_r |t - t'|) \right\} \\ &= 2D_t \tau + \frac{2v_a^2}{D_r^2} [D_r \tau + (e^{-D_r \tau} - 1)], \quad (26) \end{aligned}$$

which was used in Eq. (5). To imitate the BP model, we set $v_a = 0$ to obtain

$$\Delta r^2(\tau) = 2D_t \tau. \quad (27)$$

Note that here the dynamics of the robot does not depend on the rotational diffusion constant D_r .

-
- [1] S. Ramaswamy, The mechanics and statistics of active matter, *Annu. Rev. Condens. Matter Phys.* **1**, 323 (2010).
- [2] M. C. Marchetti, J.-F. Joanny, S. Ramaswamy, T. B. Liverpool, J. Prost, M. Rao, and R. A. Simha, Hydrodynamics of soft active matter, *Reviews of modern physics* **85**, 1143 (2013).
- [3] H. Chaté, Dry aligning dilute active matter, *Annual Review of Condensed Matter Physics* **11**, 189 (2020).
- [4] J. Toner, Y. Tu, and S. Ramaswamy, Hydrodynamics and phases of flocks, *Annals of Physics* **318**, 170 (2005).
- [5] N. Kumar, H. Soni, S. Ramaswamy, and A. Sood, Flocking at a distance in active granular matter, *Nature communications* **5**, 4688 (2014).
- [6] T. Sanchez, D. T. Chen, S. J. DeCamp, M. Heymann, and Z. Dogic, Spontaneous motion in hierarchically assembled active matter, *Nature* **491**, 431 (2012).
- [7] J. Brugués and D. Needleman, Physical basis of spindle self-organization, *Proceedings of the National Academy of Sciences* **111**, 18496 (2014).
- [8] M. E. Cates and J. Tailleur, Motility-induced phase separation, *Annu. Rev. Condens. Matter Phys.* **6**, 219 (2015).
- [9] N. Kumar, R. Zhang, S. A. Redford, J. J. de Pablo, and M. L. Gardel, Catapulting of topological defects through elasticity bands in active nematics, *Soft Matter* **18**, 5271 (2022).
- [10] J. Palacci, S. Sacanna, A. P. Steinberg, D. J. Pine, and P. M. Chaikin, Living crystals of light-activated colloidal surfers, *Science* **339**, 936 (2013).
- [11] N. Kumar, R. Zhang, J. J. De Pablo, and M. L. Gardel, Tunable structure and dynamics of active liquid crystals, *Science advances* **4**, eaat7779 (2018).
- [12] R. A. Simha and S. Ramaswamy, Hydrodynamic fluctuations and instabilities in ordered suspensions of self-propelled particles, *Physical review letters* **89**, 058101 (2002).
- [13] Y. Hatwalne, S. Ramaswamy, M. Rao, and R. A. Simha, Rheology of active-particle suspensions, *Physical review letters* **92**, 118101 (2004).
- [14] S. Rafai, L. Jibuti, and P. Peyla, Effective viscosity of microswimmer suspensions, *Physical Review Letters* **104**, 098102 (2010).
- [15] H. M. López, J. Gachelin, C. Douarche, H. Auradou, and E. Clément, Turning bacteria suspensions into superfluids, *Physical review letters* **115**, 028301 (2015).
- [16] M. Fruchart, C. Scheibner, and V. Vitelli, Odd viscosity and odd elasticity, *Annual Review of Condensed Matter Physics* **14**, 471 (2023).
- [17] L. M. Nash, D. Kleckner, A. Read, V. Vitelli, A. M. Turner, and W. T. Irvine, Topological mechanics of gyroscopic metamaterials, *Proceedings of the National Academy of Sciences* **112**, 14495 (2015).
- [18] M. Brandenbourger, X. Locsin, E. Lerner, and C. Coullais, Non-reciprocal robotic metamaterials, *Nature communications* **10**, 4608 (2019).
- [19] A. Souslov, B. C. Van Zuiden, D. Bartolo, and V. Vitelli, Topological sound in active-liquid metamaterials, *Nature Physics* **13**, 1091 (2017).
- [20] G. R. Gossweiler, C. L. Brown, G. B. Hewage, E. Sapiro-Gheiler, W. J. Trautman, G. W. Welshofer, and S. L. Craig, Mechanochemically active soft robots, *ACS applied materials & interfaces* **7**, 22431 (2015).
- [21] A. Unruh, A. M. Brooks, I. S. Aranson, and A. Sen, Programming motion of platinum microparticles: From linear to orbital, *ACS Applied Engineering Materials* (2023).
- [22] R. Zhang, S. A. Redford, P. V. Ruijgrok, N. Kumar, A. Mozaffari, S. Zemsky, A. R. Dinner, V. Vitelli, Z. Bryant, M. L. Gardel, and J. J. de Pablo, Spatiotemporal control of liquid crystal structure and dynamics through activity patterning, *Nature Materials* **20**, 875 (2021).
- [23] I. Buttinoni, G. Volpe, F. Kümmel, G. Volpe, and C. Bechinger, Active brownian motion tunable by light, *Journal of Physics: Condensed Matter* **24**, 284129 (2012).
- [24] S. Li, R. Batra, D. Brown, H.-D. Chang, N. Ranganathan, C. Hoberman, D. Rus, and H. Lipson, Particle robotics based on statistical mechanics of loosely coupled components, *Nature* **567**, 361 (2019).
- [25] M. A. Fernandez-Rodriguez, F. Grillo, L. Alvarez, M. Rathlef, I. Buttinoni, G. Volpe, and L. Isa, Feedback-controlled active brownian colloids with space-dependent rotational dynamics, *Nature communications* **11**, 4223 (2020).
- [26] S. G. Prasath, S. Mandal, F. Giardina, J. Kennedy, V. N. Murthy, and L. Mahadevan, Dynamics of cooperative excavation in ant and robot collectives, *Elife* **11**, e79638 (2022).
- [27] F. Siebers, A. Jayaram, P. Blümler, and T. Speck, Exploiting compositional disorder in collectives of light-driven circle walkers, *Science Advances* **9**, eadf5443 (2023).
- [28] B. Nakayama, H. Nagase, H. Takahashi, Y. Saito, S. Hatayama, K. Makino, E. Yamamoto, and T. Saiki, Tunable pheromone interactions among microswimmers,

- Proceedings of the National Academy of Sciences **120**, e2213713120 (2023).
- [29] N. Aubert-Kato, C. Fosseprez, G. Gines, I. Kawamata, H. Dinh, L. Cazenille, A. Estevez-Tores, M. Hagiya, Y. Rondelez, and N. Bredeche, Evolutionary optimization of self-assembly in a swarm of bio-micro-robots, in *Proceedings of the Genetic and Evolutionary Computation Conference* (2017) pp. 59–66.
- [30] Z. Zeravcic, V. N. Manoharan, and M. P. Brenner, Colloquium: Toward living matter with colloidal particles, *Reviews of Modern Physics* **89**, 031001 (2017).
- [31] R. Zhang, S. A. Redford, P. V. Ruijgrok, N. Kumar, A. Mozaffari, S. Zemsky, A. R. Dinner, V. Vitelli, Z. Bryant, M. L. Gardel, *et al.*, Spatiotemporal control of liquid crystal structure and dynamics through activity patterning, *Nature materials* **20**, 875 (2021).
- [32] L. M. Lemma, M. Varghese, T. D. Ross, M. Thomson, A. Baskaran, and Z. Dogic, Spatiotemporal patterning of extensile active stresses in microtubule-based active fluids, arXiv preprint arXiv:2209.06277 (2022).
- [33] M. Rubenstein, A. Cornejo, and R. Nagpal, Programmable self-assembly in a thousand-robot swarm, *Science* **345**, 795 (2014).
- [34] A. Deblais, T. Barois, T. Guerin, P.-H. Delville, R. Vaudaine, J. S. Lintuvuori, J.-F. Boudet, J.-C. Baret, and H. Kellay, Boundaries control collective dynamics of inertial self-propelled robots, *Physical review letters* **120**, 188002 (2018).
- [35] X. Yang, C. Ren, K. Cheng, and H. Zhang, Robust boundary flow in chiral active fluid, *Physical Review E* **101**, 022603 (2020).
- [36] A. Dmitriev, A. Rozenblit, V. Porvatov, A. Molodtsova, E. Puhtina, O. Burmistrov, D. Filonov, A. Souslov, and N. Olekhno, Statistical correlations in active matter based on robotic swarms, in *2021 International Conference Engineering and Telecommunication (En&T)* (IEEE, 2021) pp. 1–3.
- [37] L. Giomi, N. Hawley-Weld, and L. Mahadevan, Swarming, swirling and stasis in sequestered bristle-bots, *Proceedings of the Royal Society A: Mathematical, Physical and Engineering Sciences* **469**, 20120637 (2013).
- [38] G. Wang, T. V. Phan, S. Li, M. Wombacher, J. Qu, Y. Peng, G. Chen, D. I. Goldman, S. A. Levin, R. H. Austin, *et al.*, Emergent field-driven robot swarm states, *Physical review letters* **126**, 108002 (2021).
- [39] M. Leyman, F. Ogemark, J. Wehr, and G. Volpe, Tuning phototactic robots with sensorial delays, *Physical Review E* **98**, 052606 (2018).
- [40] F. Arvin, J. Espinosa, B. Bird, A. West, S. Watson, and B. Lennox, Mona: an affordable mobile robot for swarm robotic applications, in *UK-RAS Conference on Robotics and Autonomous Systems* (2017) pp. 49–52.
- [41] S. K. Malu and J. Majumdar, Kinematics, localization and control of differential drive mobile robot, *Global Journal of Research In Engineering* (2014).
- [42] J. R. Howse, R. A. Jones, A. J. Ryan, T. Gough, R. Vafabakhsh, and R. Golestanian, Self-motile colloidal particles: from directed propulsion to random walk, *Physical review letters* **99**, 048102 (2007).
- [43] C. Bechinger, R. Di Leonardo, H. Löwen, C. Reichhardt, G. Volpe, and G. Volpe, Active particles in complex and crowded environments, *Reviews of Modern Physics* **88**, 045006 (2016).
- [44] J. Tailleur and M. Cates, Statistical mechanics of interacting run-and-tumble bacteria, *Physical review letters* **100**, 218103 (2008).
- [45] A. P. Solon, M. E. Cates, and J. Tailleur, Active brownian particles and run-and-tumble particles: A comparative study, *The European Physical Journal Special Topics* **224**, 1231 (2015).
- [46] H. C. Berg and D. A. Brown, Chemotaxis in escherichia coli analysed by three-dimensional tracking, *Nature* **239**, 500 (1972).
- [47] N. Kumar, R. K. Gupta, H. Soni, S. Ramaswamy, and A. Sood, Trapping and sorting active particles: Motility-induced condensation and smectic defects, *Physical Review E* **99**, 032605 (2019).
- [48] L. Angelani, Averaged run-and-tumble walks, *Europhysics Letters* **102**, 20004 (2013).
- [49] G. M. Viswanathan, M. G. Da Luz, E. P. Raposo, and H. E. Stanley, *The physics of foraging: an introduction to random searches and biological encounters* (Cambridge University Press, 2011).
- [50] E. Bonabeau, M. Dorigo, and G. Theraulaz, Inspiration for optimization from social insect behaviour, *Nature* **406**, 39 (2000).
- [51] O. Feinerman, I. Pinkoviezky, A. Gelblum, E. Fonio, and N. S. Gov, The physics of cooperative transport in groups of ants, *Nature Physics* **14**, 683 (2018).
- [52] A. Pal, L. Kuśmierz, and S. Reuveni, Search with home returns provides advantage under high uncertainty, *Physical Review Research* **2**, 043174 (2020).
- [53] A. Kaiser, H. Wensink, and H. Löwen, How to capture active particles, *Physical review letters* **108**, 268307 (2012).
- [54] R. Di Leonardo, L. Angelani, D. Dell’Arciprete, G. Ruocco, V. Iebba, S. Schippa, M. P. Conte, F. Mecarini, F. De Angelis, and E. Di Fabrizio, Bacterial ratchet motors, *Proceedings of the National Academy of Sciences* **107**, 9541 (2010).
- [55] S. Mandal, How do animals find their way back home? a brief overview of homing behavior with special reference to social hymenoptera, *Insectes sociaux* **65**, 521 (2018).
- [56] M. R. Evans and S. N. Majumdar, Diffusion with stochastic resetting, *Physical review letters* **106**, 160601 (2011).
- [57] A. Pal and S. Reuveni, First passage under restart, *Physical review letters* **118**, 030603 (2017).
- [58] O. Tal-Friedman, A. Pal, A. Sekhon, S. Reuveni, and Y. Roichman, Experimental realization of diffusion with stochastic resetting, *The journal of physical chemistry letters* **11**, 7350 (2020).
- [59] A. Chechkin and I. Sokolov, Random search with resetting: a unified renewal approach, *Physical review letters* **121**, 050601 (2018).
- [60] V. Balakrishnan, *Elements of nonequilibrium statistical mechanics*, Vol. 3 (Springer, 2008).
- [61] V. Balakrishnan, On a simple derivation of master equations for diffusion processes driven by white noise and dichotomic markov noise, *Pramana* **40**, 259 (1993).
- [62] I. Santra, U. Basu, and S. Sabhapandit, Run-and-tumble particles in two dimensions: Marginal position distributions, *Physical Review E* **101**, 062120 (2020).
- [63] U. Basu, S. N. Majumdar, A. Rosso, and G. Schehr, Active brownian motion in two dimensions, *Physical Review E* **98**, 062121 (2018).